

Imitating dolphins: Impact of active boundary modulation on near-boundary velocity in channel flow

Silvia Matt (✉ silvia.matt@nrlssc.navy.mil)

United States Naval Research Laboratory

Weilin Hou

United States Naval Research Laboratory

Austin Thombs

United States Naval Research Laboratory

Hongyang Shi

Michigan State University

Thassyo Pinto

Michigan State University

Xiaobo Tan

Michigan State University

Article

Keywords: Boundary layer control, Boundary actuation, Particle Image Velocimetry, Numerical tank, Channel flow

Posted Date: March 11th, 2022

DOI: <https://doi.org/10.21203/rs.3.rs-1428649/v1>

License:   This work is licensed under a Creative Commons Attribution 4.0 International License.

[Read Full License](#)

Abstract

Recent advances in technology have renewed the interest in the impact of viscoelastic boundaries and active boundary modulation on hydrodynamic drag and boundary layer turbulence. Viscoelastic boundary materials, such as found in dolphin skin, have the potential to reduce frictional drag by delaying the transition from laminar to turbulent flow in the boundary layer around the body and minimizing turbulence. Possible mechanisms to reduce boundary layer turbulence include counteracting coherent structures or impacting momentum near the boundary. Actuating a deformable membrane in channel flow allows the investigation of the impact of boundary actuation on boundary layer turbulence for a range of actuation parameters and flow channel speeds. We developed a deformable boundary and tested the system in channel flow, in direct contact with the water, actuating at various wave patterns and frequencies. The impact on boundary layer velocity was investigated with Particle Image Velocimetry. Numerical simulations from a companion model complement and support experimental results. Boundary actuation is shown to impact the boundary layer velocity profile and frictional drag, and to reduce near-boundary shear in the region of actuation. Achieving a reduction of boundary layer turbulence in a natural environment could lead to more energy-efficient platforms and underwater vehicles.

1. Introduction

The interest in the impact of viscoelastic boundary materials and active boundary modulation on hydrodynamic drag and boundary layer turbulence dates back to the 1930s, when Gray [1] first linked the superior hydrodynamic capabilities of dolphins to the viscoelastic properties of their skin. His work prompted increased interest in the study of boundary layer drag and transition to turbulence near compliant boundaries, a lot of which is discussed in [2]. Viscoelastic boundary materials, such as dolphin skin, and boundary roughness elements, such as shark skin denticles, are known to have the potential to reduce skin friction drag, by delaying the transition from laminar to turbulent flow in the boundary layer around the body or by minimizing boundary layer turbulence. In the former, a laminar boundary layer is prevented from becoming turbulent by adding boundary modulations to counteract the first instabilities to develop, the so-called Tollmien-Schlichting (TS) waves [3][4]. These boundary instabilities develop as two-dimensional disturbances [5]. To prevent these instabilities from becoming fully turbulent, fluctuations can be generated on the boundary to produce a sort of counter-wave, to reduce the amplitude of the TS waves or cancel them outright. This can delay or prevent transition to turbulence and the associated increase in frictional drag [6]. In an already turbulent boundary layer, boundary modulation can achieve a stabilizing effect by moderating boundary layer coherent structures and shear “streaks”, small counter-rotating vortices that develop in the buffer zone between the viscous sublayer and the developed turbulence in the interior. This mechanism is suggested in [7] to explain why the addition of elastic boundary conditions, such as a monolayer surfactant at the air-sea interface, leads to a reduction in near-surface turbulence [8]. Recent work by [9] shows that near a free-slip boundary, i.e., an air-water

interface, high-frequency pulsations can reduce boundary friction by impacting the vorticity and momentum profile.

Technological advances in the past 5–10 years, especially in the fields of soft robotics, micro-electronics and additive manufacturing, have renewed the interest in the impact of viscoelastic boundaries and active boundary modulation on hydrodynamic drag and boundary layer turbulence. In this paper, we describe the implementation of a deformable flexible membrane, realized via a 5 x 5 actuator array, as part of the wall of a flow channel and in direct contact with the water, to study the impact of boundary modulation on channel flow dynamics (Fig. 1). The deformable boundary, which can be actuated at various wave patterns and frequencies, is installed in the laminar-to-turbulent flow tank flowSiTTE, part of the Simulated Turbulence and Turbidity Environment (SiTTE) at the Naval Research Laboratory NRL Stennis Space Center (NRL SSC) [10][11]. Results show that boundary layer velocity is decreased with actuation under the actuated membrane, consistent with reduced frictional drag, in particular at higher free stream velocity and actuation frequency. Velocity profiles and vorticity near the boundary are modified by the actuation, and turbulent stresses are shown to be increased under the region of actuation, as well as in its wake. Numerical simulations corroborate the laboratory results and predict a reduction of drag of up to 10% under the region of actuation for certain actuation parameters. Achieving a reduction of boundary layer turbulence for in-water vehicles and other platforms would have profound implications for propulsion and energy efficiency.

2. Results

2.1. Laboratory experiments

To investigate the potential of active boundary modulation to mitigate boundary layer turbulence and thus reduce frictional drag, we ran a set of experiments generating boundary actuation patterns as both streamwise and transverse waves with different wave frequencies and flow speeds.

Under “slow” free-stream flow conditions, $U_0 = 0.09$ m/s, where the flow is not expected to be fully turbulent, we see no change in velocity with actuation in the wake region past the actuated boundary. Directly under the actuated boundary, near boundary velocity shows a slight decrease at the highest actuation frequency (Fig. 2). A reduction in near-boundary velocity relates to a decrease in shear at the boundary and is consistent with a reduction in frictional drag.

For “fast” free-stream flow conditions, with $U_0 = 0.55$ m/s, and a more turbulent boundary layer, velocity measurements taken in the wake past the actuated boundary, at location $x = 25$ mm (see Section 4), show that boundary actuation impacts the near-boundary velocity profile, including the log layer region of the profile (Fig. 3). At this measurement location, we see increased velocity with respect to the control consistent with an expected increase in shear. In contrast, measurements directly under the actuated boundary show a decrease in boundary velocity with actuation. This result is consistent with an expected decrease in frictional drag on the actuated boundary, as shown in the numerical simulations (see 2.2).

A look at the velocity fields and near-boundary flow structure helps put the impact on the velocity profiles into the context of near-boundary dynamics. As shown in Fig. 4, the velocity vector under the actuated membrane is directed downward, indicating vortices and disturbance to the velocity at spatial scales of several centimeters, reaching beyond the boundary layer into the flow interior. This flow pattern suggests that the mechanisms at play may be similar to those recently reported in [9]. In their experiments of air pulsating onto a water boundary at high frequencies, momentum is redistributed in the boundary layer under the pulsation, which in turn impacts friction and near-boundary turbulence.

A full comparison to the results by [9], and the calculation of a full momentum budget, is beyond the scope of this article. However, in a more limited comparison to their work, we find our results to be consistent with their experiments on turbulent flow near an oscillating free-slip boundary. When calculating turbulent stress terms, estimated via the triple decomposition described in Section 4, the turbulent stresses are enhanced under the region of boundary actuation, and in its wake (Fig. 5) for fast flow conditions.

We further calculated the non-dimensionalized viscous shear stress profiles for control and actuation (10 Hz actuation) under fast flow conditions (i.e., $U_0 = 0.55$ m/s), at the locations directly under and in the wake of the actuated region (Fig. 6). The viscous shear stress in a turbulent boundary layer peaks at the wall and transfers streamwise momentum, as indicated in [9]. We find that the peak of the viscous shear stress is shifted away from the wall in all cases. Due to limitations in near-boundary resolution, we are unable to confirm a reduction of viscous shear stress with actuation on the actuated boundary in this data set. Nevertheless, the profile shape, in particular in the wake region, suggests a pattern comparable to that reported in [9], consistent with an impact on streamwise momentum in the boundary layer.

2.2. Numerical experiments

The laboratory experiments are augmented by numerical simulations emulating the laboratory setup. The numerical experiments allow exploration of the parameter space in terms of actuation amplitude, wavelength, and frequency and provide complete fields of velocity to aid interpretation of laboratory results.

Visualizing boundary vortices by calculating the so-called Λ^2 criterion, a standard measure of vortical structures, boundary actuation is found to impact near boundary coherent structures, including the shedding of hairpin vortices (Supplementary material 1). Instantaneous fields of shear stress at the tank lid boundary show prominent “streak-like” features, indicative of near-boundary coherent structures in the flow past the lip, which is designed to “trip” the flow from laminar to turbulent (Fig. 7, also see Section 4 for model configuration). Such streaks are well-known features of the shear-driven boundary layer and can exist near solid and flexible boundaries [12][13]. All actuation scenarios shown in Fig. 7 are standing waves oriented in the streamwise direction. Respective actuation parameters are inset on the figure and vary in amplitude, wavelength and wave frequency. The fields of boundary shear stress were taken at a flow time of $t = 5$ s after the flow reaches a steady state. The disturbances caused by boundary modulation are visible in the region of actuation and in its wake. The strongest impact in the wake region is visible for the long wavelength - high amplitude cases, where the wavelength and amplitude were

chosen to compare to the laboratory setup. At increased mesh resolution, realized for this “lab actuation” case, shear stress is shown to be both increased and decreased under the actuated boundary, depending on the phase of the boundary deformation. Averaging these fields over the region of actuation, and over one actuation period, shear stress can be reduced by up to 10% under the actuated boundary, and is generally increased by a similar amount in the wake region.

To gain a better understanding of the three-dimensional nature of near-boundary coherent structures and turbulent dynamics, fields of velocity variance were calculated as described in Section 4.2, for a cross section at the far end of the actuated region (Fig. 8). This calculation can also be considered a proxy for turbulent fluctuations. With nearly all waveforms, there is a visible increase in the velocity variance with actuation along the upper boundary (uppermost cm). The strongest impact on deeper layers is seen at the highest actuation frequency. Turbulent fluctuations are more highly resolved at higher mesh resolution, as expected, but the relative changes between control and actuation remain, with a strong, but shallow impact, seen in the “lab actuation” case, at both mesh resolutions.

Average velocity profiles provide a direct comparison to laboratory experiments and impact of actuation on near-boundary velocity (Fig. 9). As in the laboratory experimental results, for most actuation scenarios, the near-boundary velocity under the actuated membrane is decreased with actuation, pointing to reduced friction under the membrane. In the wake region, the impact is predominantly on the velocity in the log-layer part of the profile, and again compares favourably to the results from the laboratory experiments shown in Fig. 7. The wake profiles show a slight increase in near-boundary velocity for actuation with longer wavelength, including the “lab actuation” case (which is shown in blue -*-).

A comparison between laboratory experiment and numerical simulations at the highest boundary layer mesh resolution are shown in Fig. 10.

In both laboratory experiments and numerical simulation, the boundary layer velocity is decreased with actuation under the actuated region. This is consistent with reduced shear stress, on average, over the actuated boundary. In the wake region, the velocity is increased with actuation near the wall, and shows a slight dip with respect to control in the log-layer region, both in laboratory experiments and numerical model. Overall, the model tracks well the laboratory results and thus supports the laboratory findings as well as allows the exploration of actuation parameters.

3. Discussion

We investigated the impact of boundary actuation on turbulence by implementing a deformable boundary, a 5 x 5 actuator array, overlaid by a PDMS membrane, in the tank lid of a flow channel. The actuated boundary was in direct contact with the flow and can be actuated at various wave patterns and frequencies. Velocity fields were obtained with PIV near the actuated boundary in the flow channel for slow and fast flow for a range of actuation parameters. Boundary actuation was shown to impact the boundary layer velocity profile and near boundary turbulent and viscous stresses. Consistent with results reported near a pulsating free-slip (air-water) boundary, the boundary layer velocity under the actuated

membrane is decreased with actuation and increased after the membrane, for the fast flow, higher actuation frequency case. Velocity profiles and vorticity near the boundary are modified by the actuation, with vortices pushing away from the wall and thus the potential of the actuation to interact with the velocity in or beyond the log layer region of the flow. These results are consistent with those from the companion numerical model. In the numerical model, shear stress averaged over the actuated region and over one wave period can be reduced by as much as 10%, which directly translates to a reduction in skin friction drag. In the region of flow downstream of actuation, shear stress increases compared to the control. Velocity variance also increases, in particular with high amplitude actuation. Correspondingly, in the laboratory results, turbulent stresses are increased under the actuated membrane and in the wake of actuation and the peak of the viscous shear stress profile is shifted up and away from the wall, both consistent with recent findings in literature, and suggesting an impact of boundary pulsation on the momentum profile. The detailed analysis by [9], which is beyond the scope of this paper, showed that for their setup of turbulent flow under a pulsating free-slip boundary, at high pulsation frequency, the oscillation can act as a momentum source, and the associated pumping effect may explain reduced skin friction under the region of actuation. Our results suggest that similar dynamics are at play under the oscillating no-slip boundary presented here, and more in-depth laboratory experiments and analysis will be the subject of future work. The work presented in this paper contributes to the development of methods to reduce boundary layer instabilities, which has important implications for drag reduction and could lead to more energy-efficient platforms and vehicles.

4. Methods: Laboratory Setup And Numerical Model

4.1. Laboratory Setup and Analysis

Experiments investigating the impact of boundary actuation at various patterns and frequencies on near boundary velocity and turbulence were set up at the flowSiTTE flow channel, the laminar-to-turbulent flow tank of the Simulated Turbulence and Turbidity (SiTTE) facility at NRL SSC. The SiTTE facility consists of a large Rayleigh-Bénard convective tank, and the smaller flow channel with a working section of 0.6 m by 0.2 m by 0.2 m, capable of flow speeds up to 1.35 m/s. A detailed description of the SiTTE convective laboratory and companion numerical tank can be found in [10]. A deformable membrane system, a 5 x 5 array of voice coil motors (VCM) overlaid by a flexible polydimethylsiloxane (PDMS) membrane was integrated in the tank lid of the working section of the laboratory flow channel (Fig. 1, top).

The mechanical structure of this 5 x 5 VCM-actuated membrane assembly is shown in Fig. 1 (bottom). Twenty-five VCMs (NCM01-04-001-2IB, H2W Technologies, Inc.), which can be individually controlled, are clamped in a 3D-printed frame (using Stratasys J750 polyjet 3D-printer with VeroClear materials) with the motors' shaft heads embedded in the PDMS membrane (about 4.5 mm thickness; Young's modulus of about 240 kPa), forming a firm connection even under high-frequency vibration. Details of actuator control and assembly can be found in [14] and [15], respectively.

The array of 25 actuators was implemented in the lid for the flow channel working section (Supplementary material 2). The membrane covering the actuator array is in direct contact with the flow and can be controlled to deform in various wave-like patterns and at various control frequencies up to 10 Hz. An external control board connected to an embedded computer (Raspberry Pi 4 Model B, 4GB) via I2C communication, runs the controller script with a Python GUI to facilitate the switching between manual or automatic operation modes.

Experiments were performed in the flow tank for a range of flow speeds and membrane actuation patterns, and velocity data were collected with Particle Image Velocimetry (PIV). Waves were generated to align with the flow direction (streamwise) and in the spanwise, i.e. transverse or across-flow direction. Actuator control oscillating frequencies were set at 2 Hz, 4 Hz, and 10 Hz, corresponding to wave frequencies of 1 Hz, 2 Hz, and 5 Hz, respectively. However, the frequency setting translated to somewhat slower pulsation frequencies for the waves that were ultimately generated on the membrane. Thus, with an actuation setting for a wave with a wave frequency of $f = 5$ Hz, the frequency signal observed at measurement points in the flow near the actuated membrane was a frequency of $f = 3$ Hz. This value is used for the analysis presented here to calculate the phase-average for the velocity decomposition as described below. The control in this data set was taken with the actuator array in its resting state.

Velocity data were collected with PIV for a range of flow speed conditions, here we report measurements at “fast”, $U_0 = 0.55$ m/s and “slow”, $U_0 = 0.09$ m/s, free-stream velocities. These correspond to the slowest steady flow speed we can achieve in the tank, and an intermediate speed at which turbulence is more developed. The corresponding flow Reynolds numbers $Re = \frac{UL}{\nu}$ are $Re_{slow} = 20,000$ and $Re_{fast} = 110,000$, respectively, where U is the flow speed, L is the length scale taken as the tank height, and ν is the kinematic viscosity of water. In PIV, the flow is seeded with small buoyant particles that follow the flow. Light sheet optics on a dual-head laser fan out the laser light into a sheet that illuminates the particles in the measurement plane. A CCD (charge-coupled device) camera takes image pairs of the illuminated particles at high frequency. Velocities can then be inferred by correlating the movement of particles between successive images. Figure 11 shows the working section of the flowSiTTE tank with the PIV setup: the laser light sheet is directed upwards, in a plane parallel to the flow direction, and intercepting the top of the tank lid, where the actuated boundary is installed. The CCD camera sits perpendicular to this setup, allowing it to take images of the measurement plane. The laser is a Litron ND:Yag laser, dual cavity, 145 mJ per cavity, with a 15 Hz maximum frequency per cavity, with a wavelength of 532 nm. A light guide arm directs the light sheet into the tank, parallel to flow direction, and intersecting the tank lid and deformable boundary (Fig. 11, right). The water in the tank was seeded with silver-coated glass particles (10 μm diameter). The sampling frequency was set to 15 Hz, with an interval of 5.5 ms (slow flow) and 0.8 ms (fast flow) between laser pulses to record double frame image pairs. 1000 image pairs were collected per experiment with an image size of 2352 x 1768 pixels, with a FlowSense EO 4M-41 camera. The spatial resolution of the derived velocity field varies, as the post-processing algorithm (Dynamic Studio 6.1.3) adapts the PIV interrogation area size depending on seeding density and velocity gradients, but is on the order of mm. Here, the resolution of the resulting gridded PIV velocity field is $dx =$

dy = 0.58 mm for a field of 293 by 224 points. Figure 12 shows the Field of View (FOV) of the PIV camera at room light, and illustrates that the measurement area captures part of the deformable boundary, as well as the trailing edge behind the actuated membrane. The red and black lines in Fig. 12 indicate the locations of profile data shown in the results section of this paper. The first profile location is directly under the actuated membrane (x = - 47 mm, in PIV coordinates) and the second location is in the wake of the actuated membrane (x = 25 mm), respectively. While turbulence can be observed in the boundary layer for either flow condition, neither appears to be fully developed turbulence. This is indicated by the absence of a clear log layer in the boundary layer velocity profile, in particular for the slower flow condition (see Fig. 2). Velocity profiles as shown in Figs. 2 and 3 were averaged over all realizations (N=1000) and normalized with the respective free-stream velocity U_0 , whereas the distance from the wall, y, was normalized by the channel height H = 0.2 m.

To quantify the impact of actuation on the flow field, we calculate the phase-averaged velocities, Reynolds stresses, and the non-dimensionalized viscous shear stress, following [9]. The velocity U was decomposed into a mean velocity \bar{U} , a wave component \tilde{u} , and the fluctuating component u' :

$$U = \bar{U} + \tilde{u} + u'$$

1
Fluctuating velocity components, u' and v' , for Reynolds stresses, are calculated by subtracting the phase-averaged fields from the instantaneous velocity. For this calculation, and in the laboratory experiments, u is the horizontal, along-tank velocity, and v the vertical velocity. The prime denotes the fluctuating component. The Reynolds stress term is calculated as $\overline{u'v'}$, where the overbar denotes the time average. To calculate the profile of the viscous shear stress τ_v , the non-dimensionalized viscous shear stress is defined as follows:

$$\frac{\nu}{u_*^2} \frac{dU}{dy}$$

2
Here, ν is the kinematic viscosity of water and u_* is the friction velocity, defined as $u_* = \sqrt{\frac{\tau_w}{\rho}}$, and

estimated to be $u_* = 0.02$ m/s, an estimate confirmed by the numerical model. τ_w is the stress near the wall, and ρ is the water density. In Fig. 6, it is plotted against the normalized wall distance y^+ , defined as $\frac{yu_*}{\nu}$.

To complement the laboratory experiments and support interpretation of results, a numerical model was set up to emulate the laboratory tank, as was done previously for the convective SiTTE tank [10]. The

setup of the numerical experiments, using a Computational Fluid Dynamics (CFD) large-eddy-simulation (LES) model, is described below.

4.2. Numerical Model

The working section of the flowSiTTE tank served as the fluid domain for a numerical tank, emulating the laboratory setting. The 3D model was implemented using a Large Eddy Simulation (LES) approach, with the Smagorinsky sub-grid-scale (SGS) model [16]. The numerical model solves the filtered Navier-Stokes equations along with a turbulent viscosity term, and the continuity equation for conservation of mass. Discretization is based on the finite-element method [17]. Simulations were performed at two mesh resolutions, as shown in Fig. 13. Exploration of the parameter space was performed with the domain and mesh resolution in Fig. 13, left, key cases were solved with increased boundary layer mesh resolution (Fig. 13, right).

Domain dimensions are 0.8 m x 0.2 m x 0.1 m, in x, y, and z, respectively. A 2 mm lip is located 0.2 m from the inlet to mirror the lip present when the flow enters the test section of the flowSiTTE tank. The bottom face of the mesh was set as symmetry plane. The geometry past the lip is designed to match the 0.6 m x 0.2 m x 0.2 m dimensions of the flowSiTTE test section. The top face of the geometry is a no-slip boundary, all other boundaries are free-slip, to reduce computational requirements and wall effects. The mesh is finely resolved at the tank lid, with a boundary layer prism mesh extending approximately 3 mm from the tank lid and approximately 700,000 elements in the domain. A Moving Mesh boundary condition was implemented in the top face to simulate the actuated boundary used in the lab (Fig. 14). The boundary deformation is implemented as a wave with wavelength λ , amplitude a , and wave frequency f . In the results shown here, all wave patterns were standing waves oriented in the streamwise direction. All numerical simulations were done at “fast” free stream velocity $U_0 = 0.55$ m/s to allow for a transition to turbulent flow in the numerical model. For a more direct comparison to the laboratory experiment, we ran a “lab actuation” case with a wavelength $\lambda = 6.7$ cm, amplitude $a = 2.5$ mm, and wave frequency $f = 3$ Hz, with increased boundary layer resolution (1.2 million cells).

Figure 14 provides a detailed look at the model geometry, locations of actuated boundary and probe locations. To the bottom left of the image is the inlet, which has a normal inflow velocity of $U_0 = 0.55$ m/s, and to the upper right is the outlet. A lip with height of 2 mm extending from the tank top wall is visible 0.2 m from the inlet, running across the tank lid in the spanwise direction. The actuated region is shown in blue, and covers a 0.1 m x 0.1 m face that starts 0.2 m from the lip (0.4 m from the inlet). Boundary actuation is confined to this area. Probe locations include a cross-sectional plane, normal to the flow direction and located at the end of the actuated region (yellow), as well as a vertical profile centered in the region of actuation, indicated in red. Another profile location (green) is located 2 cm downstream of the first profile. The “wake” region (purple) is a 0.1 x 0.1 m segment directly behind the actuated region.

To quantify the impact of boundary actuation on turbulent velocity components as shown in Fig. 8, the velocity variance of the model fields was calculated as half the sum of the velocity component variances

$$k = \frac{1}{2} \left(\frac{\sum \left(u - \bar{u} \right)^2}{N} + \frac{\sum \left(v - \bar{v} \right)^2}{N} + \frac{\sum \left(w - \bar{w} \right)^2}{N} \right)$$

3

Here, u , v , and w are the velocity components in the x , y , and z direction, respectively, and N is the number of time steps over which the summation is taken. Velocity data were collected 200 times from 3–5 seconds at the steady state (i.e., at a sampling time step $\Delta t = 0.01$ s). Average velocity profiles were calculated for direct comparison to laboratory results (as in Figs. 9, 10).

Declarations

Acknowledgments. We thank Dr. Kaushik Sampath for helpful discussions on the topic. This project was supported by ONR/NRL base program 73-1G38. Numerical simulations supporting the laboratory experiments were performed on resources provided by the DoD Supercomputing Resource Center (ARL DSRC).

Competing interests. The authors declare no competing interests. **Data availability statement.** The datasets generated and/or analysed during the current study are not publicly available due the internal rules at the US Naval Research Laboratory limiting public release of data, but are available from the corresponding author on reasonable request.

Author contributions. Conceptualization: S.M; W.H. Methodology: S.M; W.H.; A.T.; H.S; T.P; X.T. Data curation: S.M.; A.T. Data visualisation: S.M.; A.T Writing original draft: S.M; All authors approved the final submitted draft.

References

1. Gray, J. (1936). Studies in animal locomotion VI. The propulsive powers of the dolphin. *J. Exp. Biol.*, 13, 192–199.
2. Babenko, V., Chun, H., and Lee, I. (2012). *Boundary Layer Flow over Elastic Surfaces. Compliant Surfaces and Combined Methods for Marine Vessel Drag Reduction*. City, State: Elsevier.
3. Tollmien, W. (1931). Grenzschichttheorie. *Handbuch der Experimentalphysik IV*, 1, Leipzig, 239–287.
4. Schlichting, H., (1929). Zur Entstehung der Turbulenz bei der Plattenströmung. *Nachr. Ges. Wiss. Göttingen, Math.-phys. Klasse*, 21–44.
5. Werlé, H. (1980). Transition and separation: Visualizations in the ONERA water tunnel. *La Recherche Aérospatiale: Bull. Bimestriel de l'Office National d'Etudes et de Recherches Aérospatiales (Paris)*, 5, 331–345.
6. Pätzold, A., Peltzer, I., and Nitsche, W. (2012). Learning from dolphin skin – active transition delay by distributed surface actuation. *Nature Inspired Fluid Mechanics, Notes on Numerical Fluid Mechanics*

and Multidisciplinary Design 119, 179–192.

7. Soloviev, A. V., Matt, S., Gilman, M., Hühnerfuss, H., Haus, B., Jeong, D., Savelyev, I., and Donelan, M. (2011). Modification of Turbulence at the Air-Sea Interface Due to the Presence of Surfactants and Implications for Gas Exchange. Part I: Laboratory Experiment. In: Gas Transfer at Water Surfaces 2010 (pp. 285–298), Kyoto University Press.
8. Matt, S., Fujimura, A., Soloviev, A., and Rhee, S. H. (2011). Modification of turbulence at the air-sea interface due to the presence of surfactants and implications for gas exchange. Part II: Numerical simulations. In: Gas Transfer at Water Surfaces 2010 (pp. 299–312), Kyoto University Press.
9. Wang, C., and Gharib, M. (2020). Effect of the dynamic slip boundary condition on the near-wall turbulent boundary layer. *J. Fluid Mech.* vol. 901, A11 (2020). doi:10.1017/jfm.2020.514
10. Matt, S., Hou, W., Goode, W., and Hellman, S. (2017). Introducing SiTTE: A controlled laboratory setting to study the impact of turbulent fluctuations on light propagation in the underwater environment. *Opt. Express* 25, 5662–5683.
11. Matt, S., Hou, W., and Goode, W. (2018). Characterizing instabilities in the developed and transitional boundary layer. *Proc. SPIE* 10631, Ocean Sensing and Monitoring X, 106310I.
12. Lesieur, M. (2008). *Turbulence in Fluids*. Springer.
13. Dhanak, M. R. and Si, C. (1999). On reduction of turbulent wall friction through spanwise wall oscillations. *J. Fluid. Mech.*, 383, 175–195.
14. Shi, H., Pinto, T., Qi, X, Coleman, D., Matt, S., Hou, W., Tan, X. (2020). Dynamic Modeling of Voice Coil Motor-Actuated Flexible Membranes. In: Proceedings of the ASME 2020 Dynamic Systems and Control Conference (DSCC2020), Pittsburgh, PA.
15. Tan X., Shi, H., Pinto, T., Coleman, D., Hou, W., Matt, S., Restaino, S., and Santiago, F. (2019). Apparatus with a controllable surface for underwater boundary flow. US patent application #16/667,089.
16. Sagaut, P. (1998). *Large Eddy Simulation for Incompressible Flows, An Introduction*. Springer.
17. COMSOL (2018). *CFD Module User's Guide, Version 5.4*. COMSOL Multiphysics.

Figures

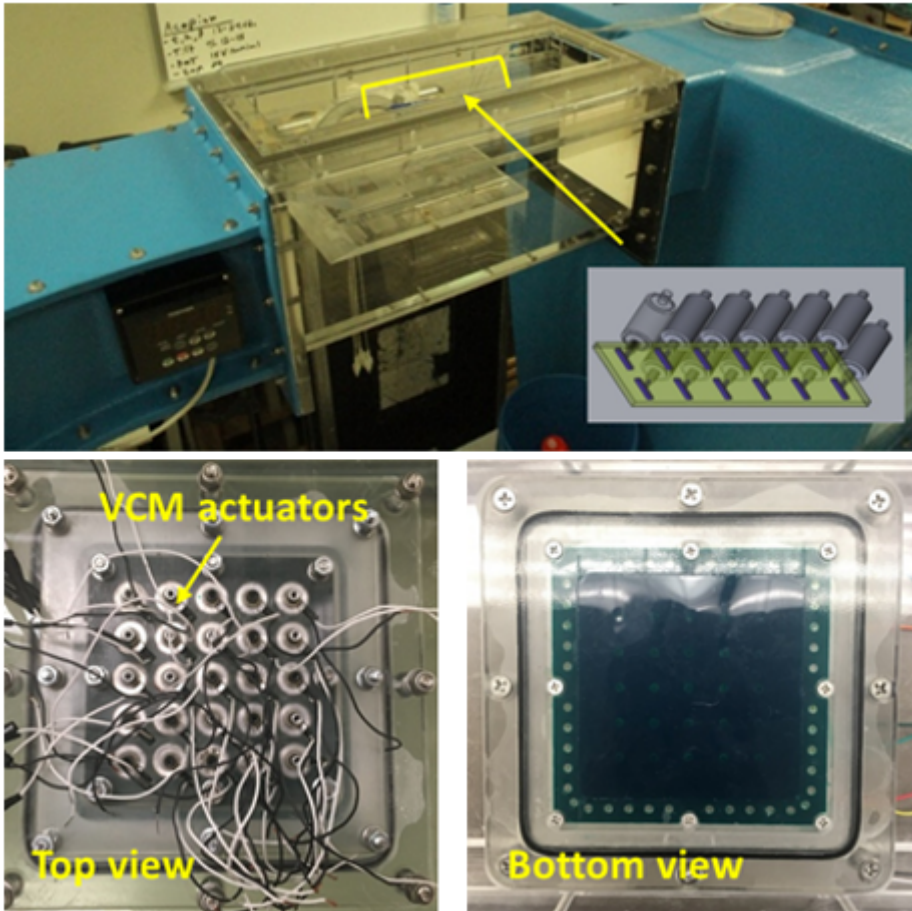


Figure 1

The top shows the working section of the flowSiTTE tank and a schematic of an actuator array for implementation in the tank lid. The bottom left shows the top of the 5 x 5 voice coil motor (VCM) actuator array and cables going to the control board. On the bottom right, the bottom view shows the PDMS membrane overlaying the actuators, which is in direct contact with the water. This deformable membrane can be actuated at various wave patterns and frequencies.

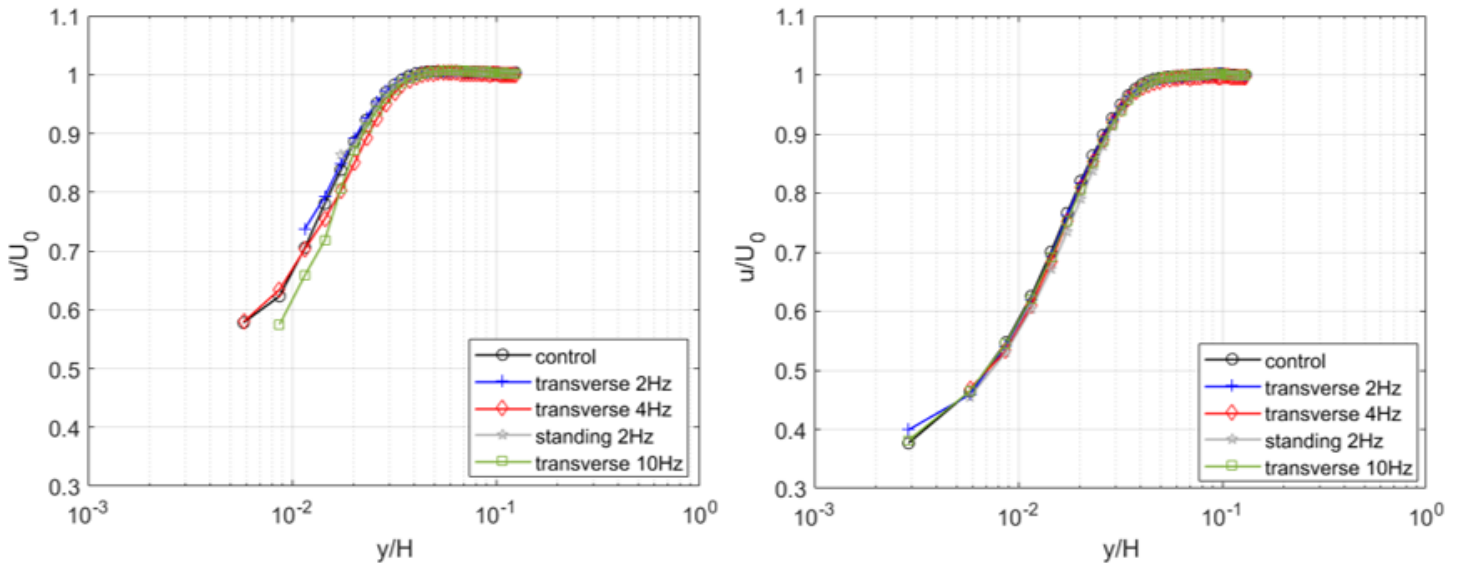


Figure 2

Velocity measurements in the region under the actuated boundary (left; taken at $x = -47$ mm, see also Fig. 12) and in the wake region (right; profile at $x = 25$ mm, see Fig. 12) for various actuation frequencies for both standing and transverse waves and for slow free-stream velocity $U_0 = 0.09$ m/s. Velocity is normalized by the free-stream velocity, and the distance from the wall, y , is normalized by channel height. Under the actuator array, wall location is chosen at $y = 48$ mm (from Particle Image Velocimetry (PIV) field of view (FOV), see Fig. 12), in the wake at $y = 50$ mm. Data quality varies between runs, due to near-boundary glare, and unresolved points were omitted.

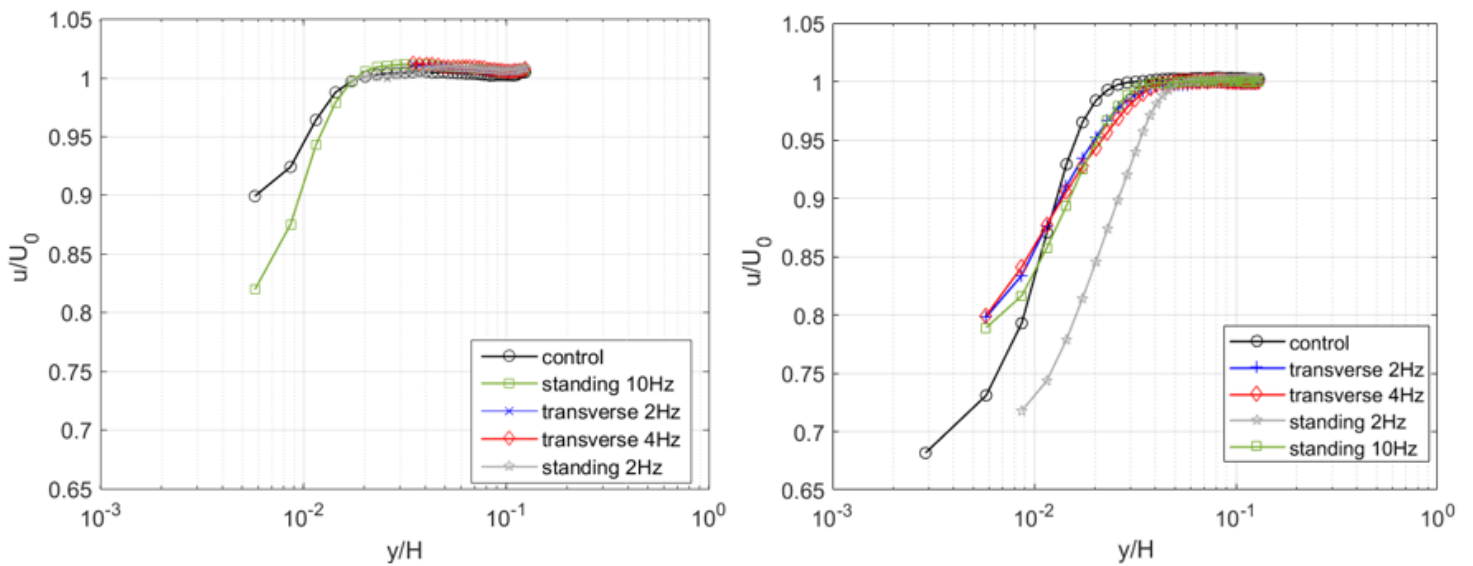


Figure 3

Velocity measurements for the case of fast free-stream velocity, $U_0 = 0.55$ m/s, in the region under the actuated boundary (left) and in the wake region (right) for various actuation frequencies. Velocity is normalized by the free-stream velocity, and the distance from the wall, y , is normalized by channel height. Data quality varies between runs, due to near-boundary glare and actuation impacting the measurement field, and unresolved points were omitted. Directly under the region of actuation, measurement quality was poor for slower actuation frequencies, due to membrane deformation interfering with the PIV measurements, and the boundary layer was unresolved in those cases (left).

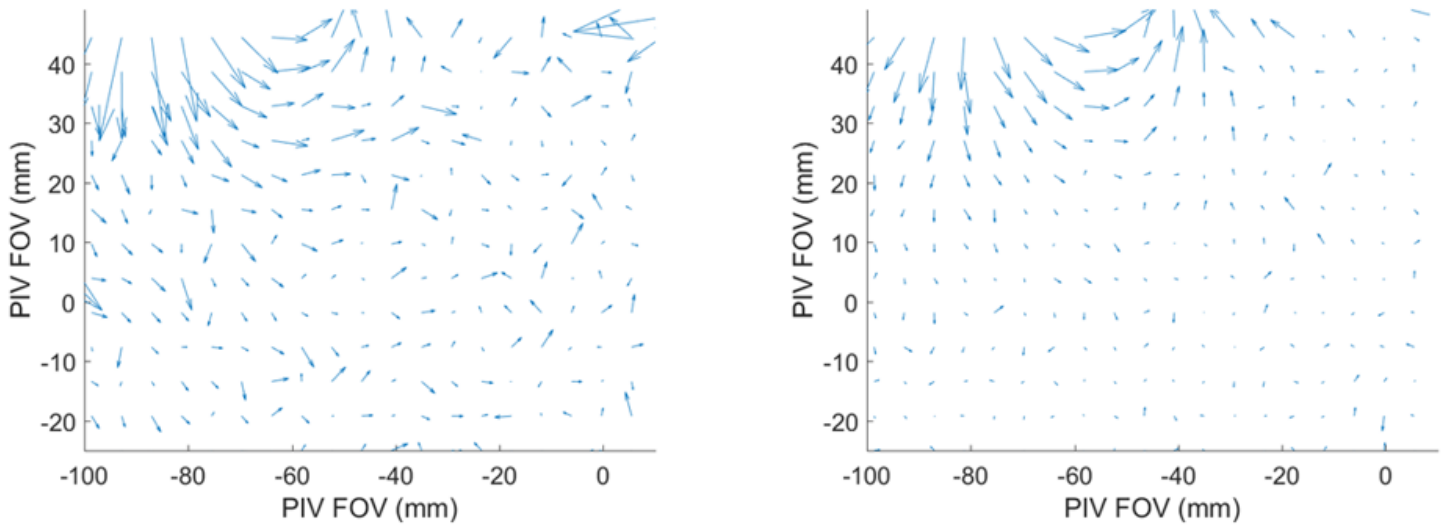


Figure 4

Two instantaneous velocity snap shots in the region of actuation during boundary movement. These were taken at different times during the experiment: left, at time $t = 2.6$ s after start of data collection, right, 85 images later, at time $t = 8.3$ s. The fields, with mean flow removed (calculated as $U - \bar{U}$

), show downward directed velocity vectors, indicating vortices under the actuated membrane with actuation. Arrows indicate velocity direction and magnitude, and the flow pattern suggests that near-boundary vorticity and momentum may be impacted by actuation, which in turn can affect near-boundary turbulence and shear.

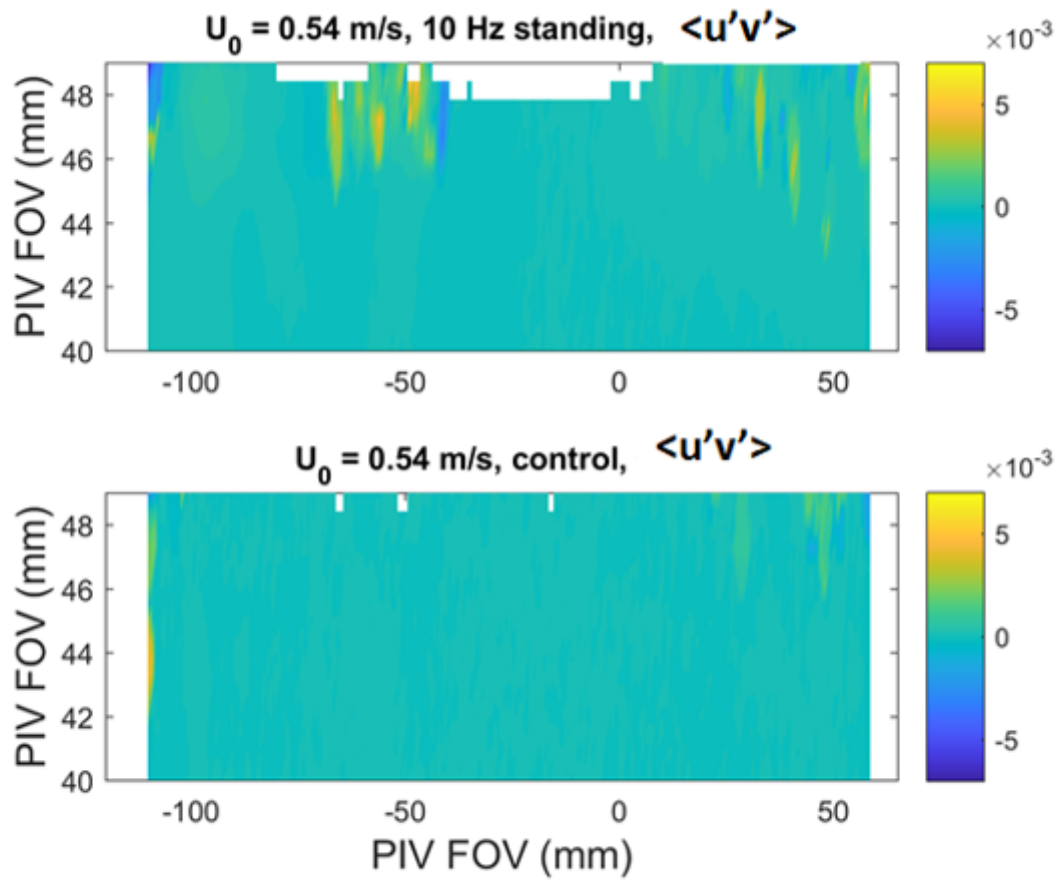


Fig. 5. Reynolds stresses, $\overline{u'v'}$, calculated after triple decomposition. The plots are for the case of fast flow, $U_0 = 0.55 \text{ m/s}$, at 10 Hz actuation (top) versus control (bottom). Actuation is shown to impact the turbulent stresses. In this case, turbulent stresses are increased under the actuation region and in its wake, consistent with results from literature.

Figure 5

See image above for figure legend.

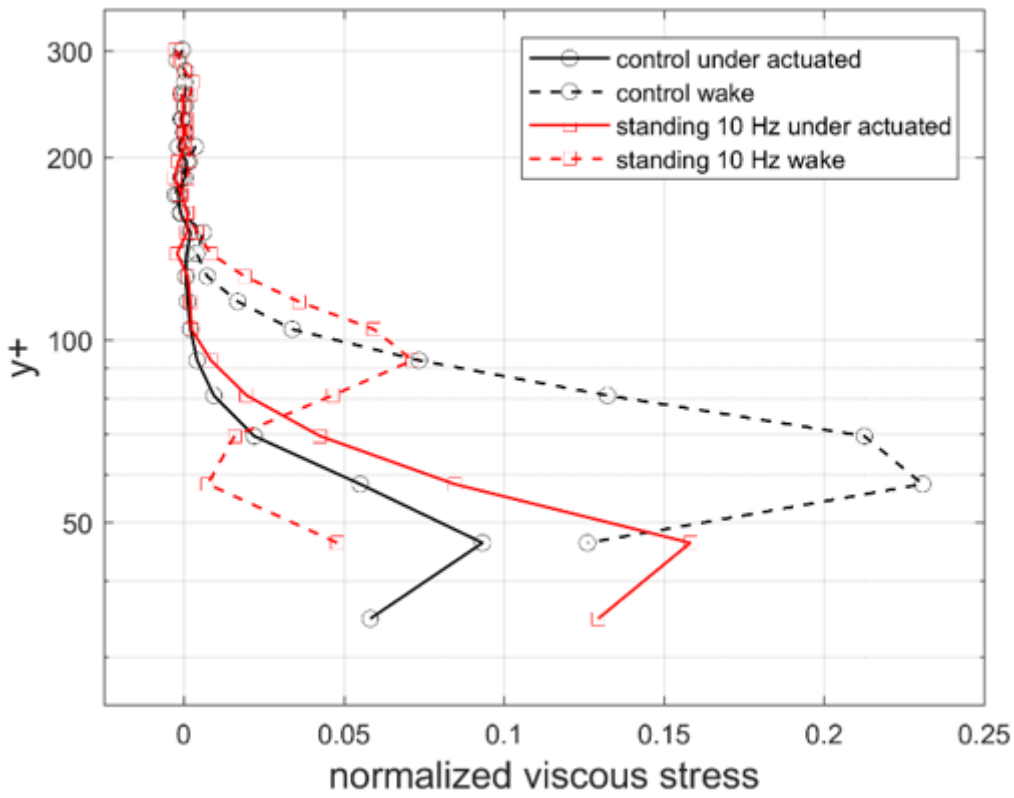


Figure 6

Non-dimensionalized viscous shear stress profiles for control (black) and actuation (red) for 10 Hz actuation in fast flow, $U_0 = 0.55$ m/s. Wake region measurement, taken at $x = 11$ mm, is dashed, and actuated region measurements are indicated by solid line.

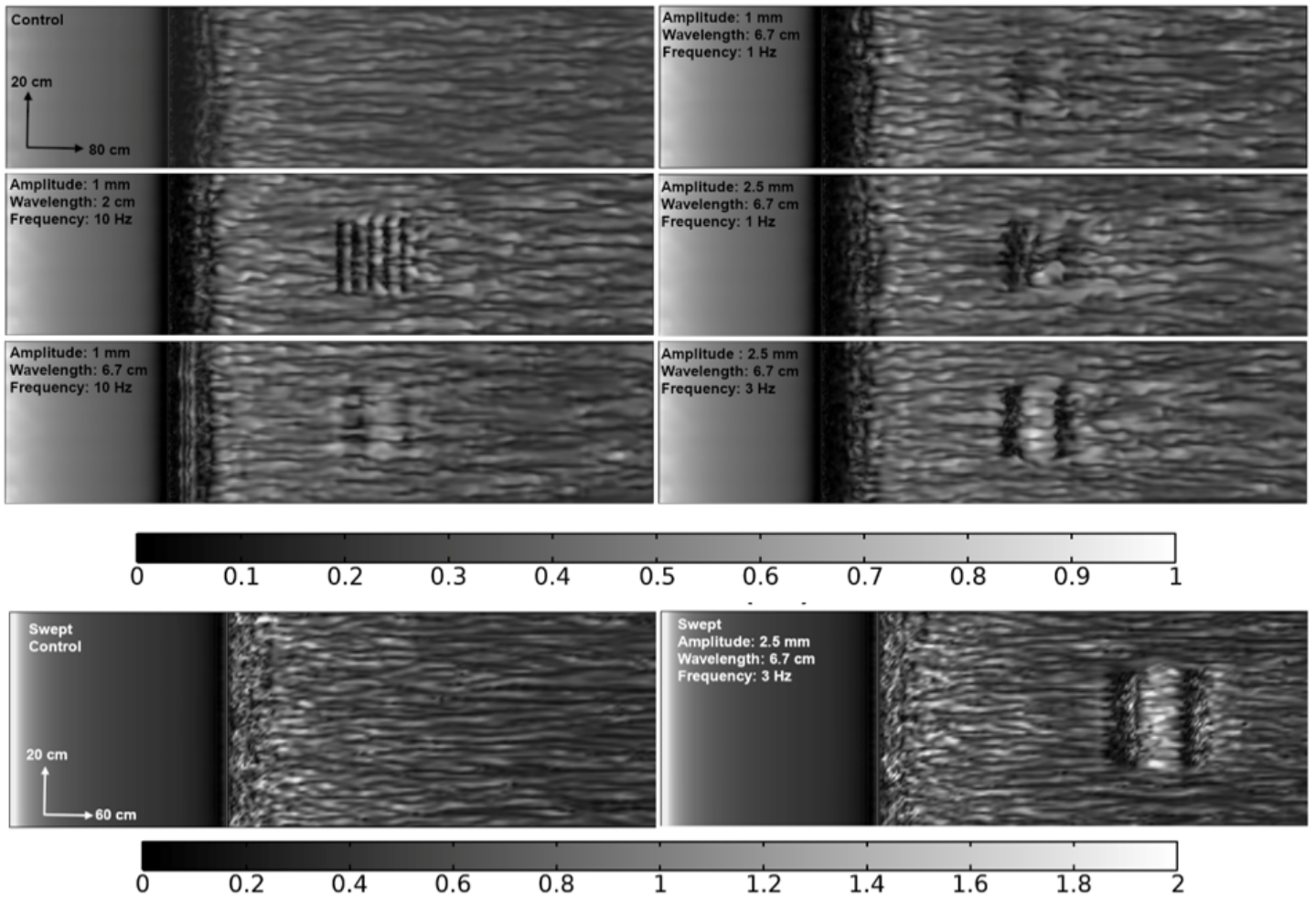


Figure 7

Plots of shear stress along the tank lid boundary for the control and a range of actuation parameters. Color range is from 0 – 1 Pa for all but the two bottom panels, for which range is from 0 – 2 Pa. Shear “streaks” characteristic of boundary layer flow form past the lip at 0.2 m from the inlet. The disturbances caused by boundary modulation are visible in the region of actuation and its wake. The two bottom right panels are the “lab actuation” case, which are directly comparable to the laboratory setup. The bottom row shows the case ran with increased near-boundary mesh resolution, the control with no actuation on the left, the key lab scenario on the right.

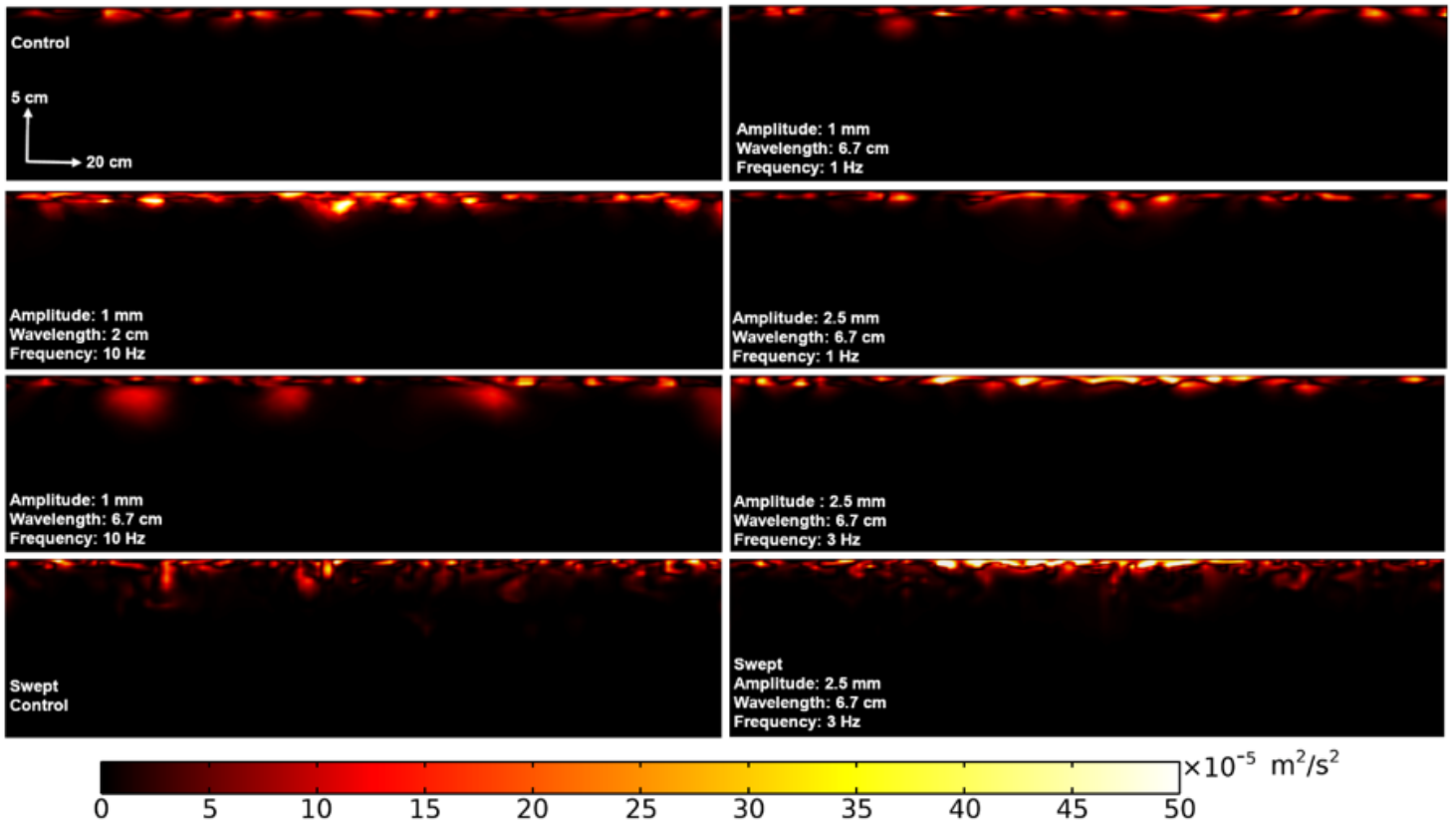


Figure 8

Sum of velocity variances as proxy for turbulent fluctuations (as in Eq. (3)) taken at the cross-section shown in yellow in Fig. 14. The colorbar ranges from 0 to $5 \cdot 10^4 \text{ m}^2/\text{s}^2$. Here, the dimensions of the section shown are 5 cm in the vertical (z) direction and 20 cm in the across tank (y) direction. The “lab actuation” case, i.e., the case most closely comparable to the laboratory experiments, has actuation parameters of $a = 2.5 \text{ mm}$, $\lambda = 6.7 \text{ cm}$ and $f = 3 \text{ Hz}$. The bottom panels show the corresponding simulations with the highest resolution (“swept”) mesh (see also Fig. 13).

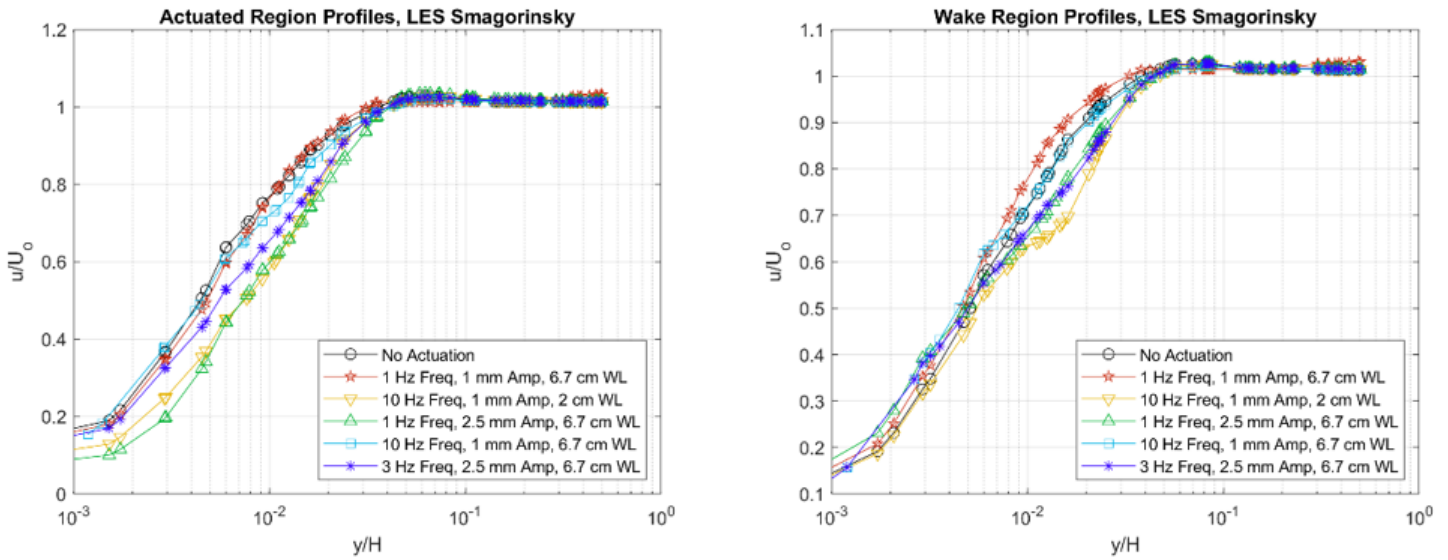


Figure 9

Velocity measurements directly under the actuated boundary (left) are contrasted with measurements past the actuated boundary (right) from the numerical model. At the wall, the velocity profiles collapse consistent with the parameterization of near-wall behavior in the LES model.

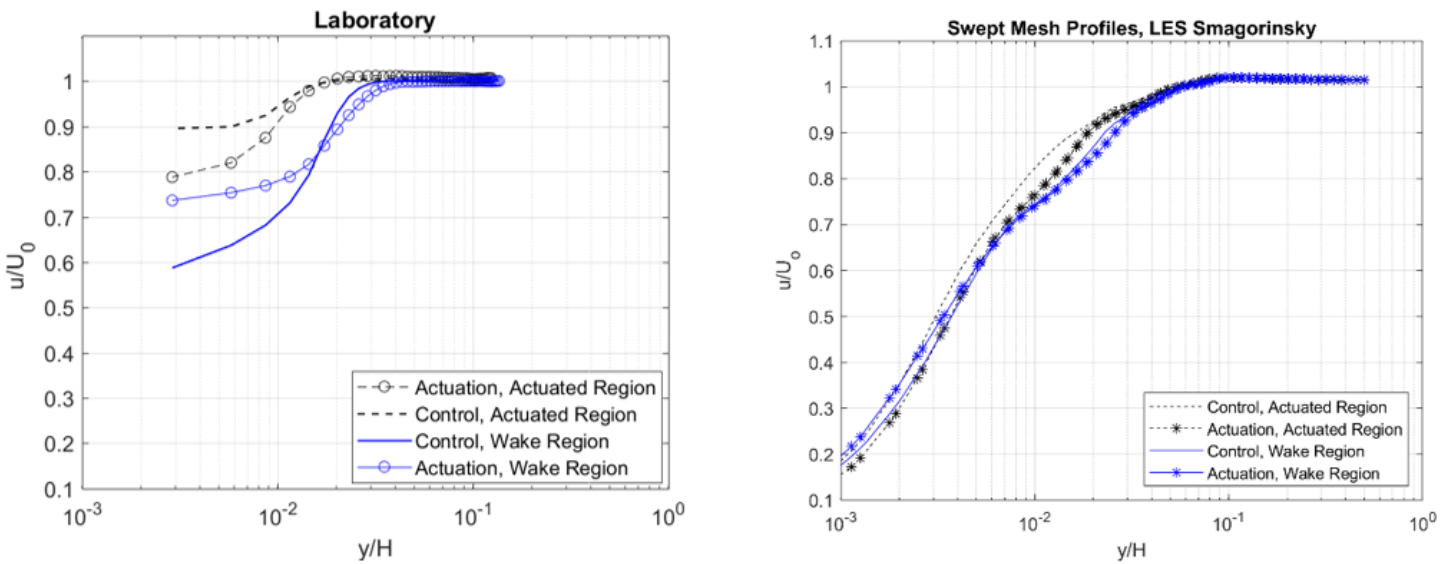


Figure 10

Velocity measurements directly under the actuated boundary are contrasted with measurements past the actuated boundary for the laboratory experiments at highest actuation frequency (left), and for the equivalent numerical “lab actuation” case (right) at high mesh resolution. Velocity is normalized as in Fig. 2ff. Under the actuated membrane, the near-boundary velocity is decreased with actuation, and increased

in its wake. Profile locations are those indicated in Fig. 12. On the right, results from the numerical simulations emulating the laboratory work. The near-wall plateau in the lab velocities is due to PIV measurement bias, but is included here to better illustrate velocity trends.

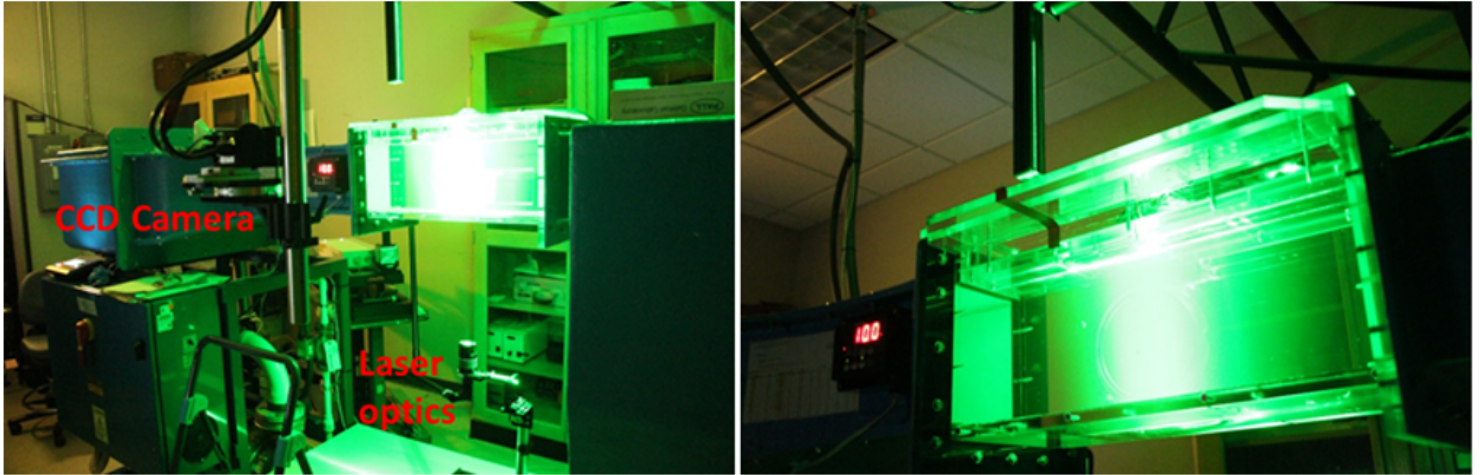


Figure 11

The flowSiTTE laboratory at NRL SSC during PIV experiments. The CCD camera and location of laser sheet optics are indicated on the left. The laser light sheet is directed upwards and aligned with the centerline of the tank, the reflection on the top boundary, as seen on the right, indicates the location of the light sheet, providing measurements of velocity for a plane in the center of the tank, and parallel to the flow direction.

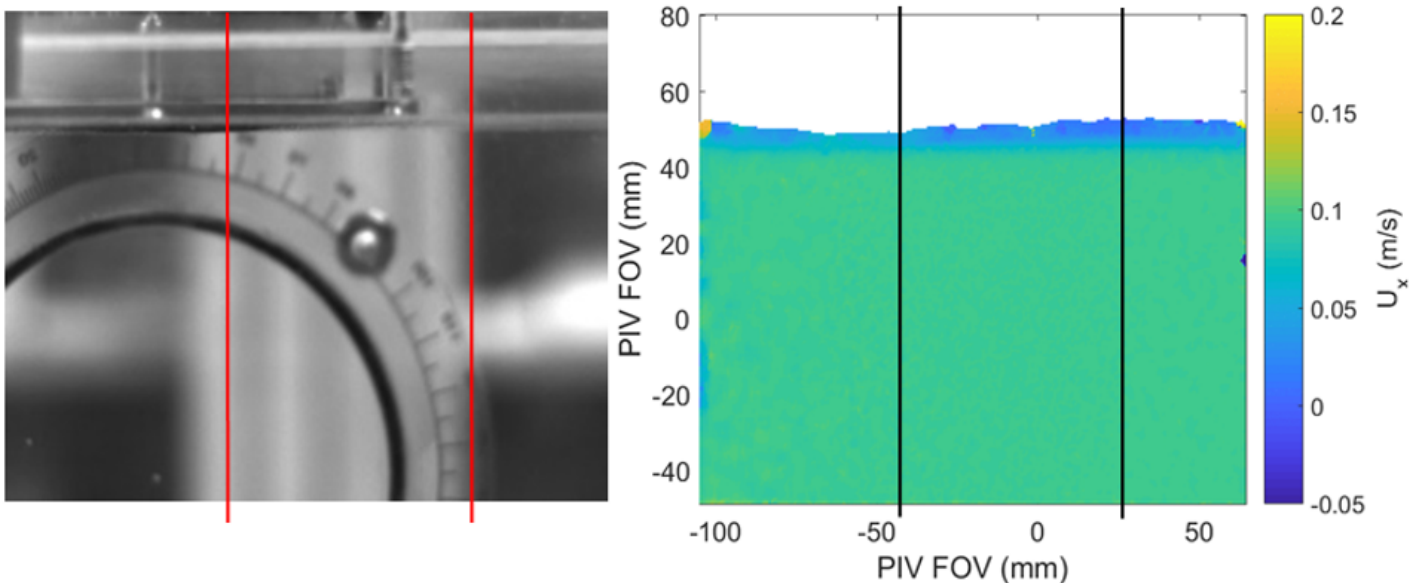


Figure 12

The image on the left was taken with the PIV camera at room light, and shows the camera's Field of View (FOV). This illustrates that the measurement area captures part of the deformable boundary, as well as the trailing edge behind the actuated membrane. On the right, an instantaneous snapshot of the corresponding velocity data from the PIV measurements is shown for the "slow" flow case, $U_0 = 0.09$ m/s. The red and black lines show the location of profile data shown in the results section of this paper, one location under the actuated membrane, at $x = -47$ mm, and the other in the wake of the actuated membrane, at $x = 25$ mm, respectively.

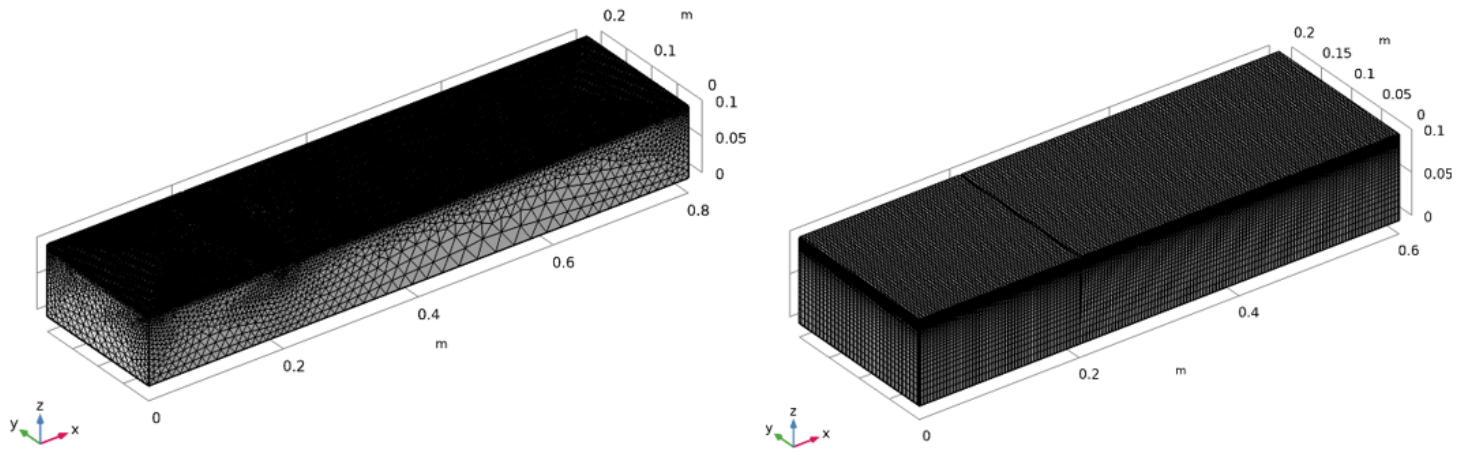


Figure 13

Domain and mesh for the numerical model. Domain dimensions on the left are 0.8 x 0.2 x 0.1 m, in the higher resolution mesh on the right, the domain is 0.6 x 0.2 x 0.1 m. A lip of thickness 2 mm extending from the tank wall into the flow is located at $x = 0.2$ m from the inlet to mirror the lip present when the flow enters the test section of the flowSiTTE tank. Exploratory simulations were performed with the mesh on the left, which is finely resolved at the tank lid, with a boundary layer prism mesh extending approximately 3 mm from the tank lid and approximately 700,000 elements in the domain. Key scenarios were simulated with the more highly resolved mesh - 1.2 million elements - shown on the right, generated as swept mesh, and using only hexahedral cells.

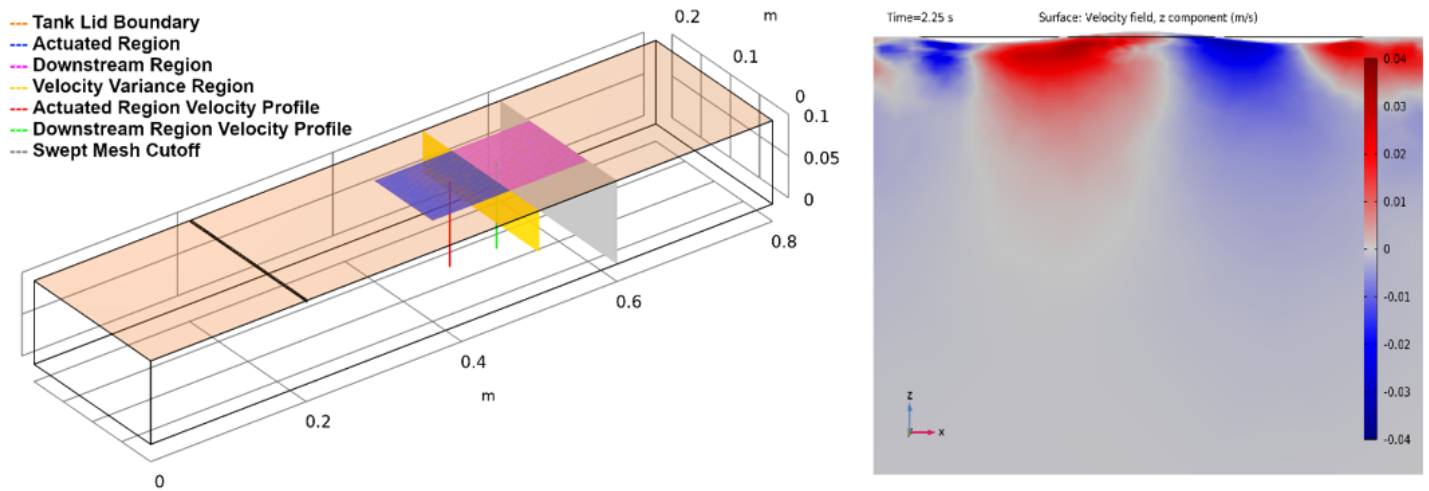


Figure 14

Locations of various data probes within the flow tank geometry. The region of actuation, indicated in blue, is a 0.1 m x 0.1 m region that starts 0.2 m from the lip (0.4 m from the inlet). Probe locations for velocity measurements are indicated in the figure. Boundary actuation is implemented via a moving mesh condition on the top boundary, as illustrated on the right.

Supplementary Files

This is a list of supplementary files associated with this preprint. Click to download.

- [SupplementaryMaterial.zip](#)